Multilayer Fresnel zone plates for high energy radiation resolve 21 nm features at 1.2 keV

Kahraman Keskinbora,[1] Anna-Lena Robisch,[2] Marcel Mayer,[1] Umut T. Sanli,[1] Corinne Grévent,[1,*] Christian Wolter,[1] Markus Weigand,[1] Adriana Szeghalmi,[3] Mato Knez,[4,5] Tim Salditt,[2] and Gisela Schütz [1]

[1]*Max Planck Institute for Intelligent Systems, Heisenbergstr. 3, 70569 Stuttgart, Germany*
[2]*Institut für Röntgenphysik, Universität Göttingen, Friedrich-Hund-Platz 1, 37077 Göttingen, Germany*
[3]*Institute of Applied Physics, Friedrich-Schiller-Universität, Max-Wien-Platz 1, 07743 Jena, Germany*
[4]*CIC nanoGUNE, Tolosa Hiribidea 76, 20018 Donostia-San Sebastian, Spain*
[5]*Ikerbasque, Basque Foundation for Science, Alameda Urquijo 36-5, 48011 Bilbao, Spain*
[*]*grevent@is.mpg.de*

Abstract: X-ray microscopy is a successful technique with applications in several key fields. Fresnel zone plates (FZPs) have been the optical elements driving its success, especially in the soft X-ray range. However, focusing of hard X-rays *via* FZPs remains a challenge. It is demonstrated here, that two multilayer type FZPs, delivered from the same multilayer deposit, focus both hard and soft X-rays with high fidelity. The results prove that these lenses can achieve at least 21 nm half-pitch resolution at 1.2 keV demonstrated by direct imaging, and sub-30 nm FWHM (full-pitch) resolution at 7.9 keV, deduced from autocorrelation analysis. Reported FZPs had more than 10% diffraction efficiency near 1.5 keV.

©2014 Optical Society of America

OCIS codes: (340.7460) X-ray microscopy; (340.0340) X-ray optics; (340.6720) Synchrotron radiation; (340.7480) X-rays, soft x-rays, extreme ultraviolet (EUV); (050.1965) Diffractive lenses; (220.4241) Nanostructure fabrication.

References and links

1. J. Vila-Comamala, Y. Pan, J. J. Lombardo, W. M. Harris, W. K. S. Chiu, C. David, and Y. Wang, "Zone-doubled Fresnel zone plates for high-resolution hard X-ray full-field transmission microscopy," J. Synchrotron Radiat. **19**(5), 705–709 (2012).
2. E. Zschech, C. Wyon, C. E. Murray, and G. Schneider, "Devices, materials, and processes for nanoelectronics: characterization with advanced x-ray techniques using lab-based and synchrotron radiation sources," Adv. Eng. Mater. **13**(8), 811–836 (2011).
3. A. Bisig, M. Stärk, M.-A. Mawass, C. Moutafis, J. Rhensius, J. Heidler, F. Büttner, M. Noske, M. Weigand, S. Eisebitt, T. Tyliszczak, B. Van Waeyenberge, H. Stoll, G. Schütz, and M. Kläui, "Correlation between spin structure oscillations and domain wall velocities," Nat. Commun. **4**, 2328 (2013).
4. M. Kammerer, H. Stoll, M. Noske, M. Sproll, M. Weigand, C. Illg, G. Woltersdorf, M. Fähnle, C. Back, and G. Schütz, "Fast spin-wave-mediated magnetic vortex core reversal," Phys. Rev. B **86**(13), 134426 (2012).
5. J. Kirz and C. Jacobsen, "The history and future of X-ray microscopy," J. Phys. Conf. Ser. **186**, 012001 (2009).
6. P. Kirkpatrick and A. V. Baez, "Formation of optical images by X-Rays," J. Opt. Soc. Am. **38**(9), 766–774 (1948).
7. S. Matsuyama, T. Wakioka, N. Kidani, T. Kimura, H. Mimura, Y. Sano, Y. Nishino, M. Yabashi, K. Tamasaku, T. Ishikawa, and K. Yamauchi, "One-dimensional Wolter optics with a sub-50 nm spatial resolution," Opt. Lett. **35**(21), 3583–3585 (2010).
8. K. Yamauchi, H. Mimura, T. Kimura, H. Yumoto, S. Handa, S. Matsuyama, K. Arima, Y. Sano, K. Yamamura, K. Inagaki, H. Nakamori, J. Kim, K. Tamasaku, Y. Nishino, M. Yabashi, and T. Ishikawa, "Single-nanometer focusing of hard x-rays by Kirkpatrick-Baez mirrors," J. Phys. Condens. Matter **23**(39), 394206 (2011).
9. S. Matsuyama, N. Kidani, H. Mimura, Y. Sano, Y. Kohmura, K. Tamasaku, M. Yabashi, T. Ishikawa, and K. Yamauchi, "Hard-X-ray imaging optics based on four aspherical mirrors with 50 nm resolution," Opt. Express **20**(9), 10310–10319 (2012).
10. D. T. Attwood, *Soft X-rays and Extreme Ultraviolet Radiation: Principles and Applications* (Cambridge University Press, 2000).
11. J. Kirz, "Phase zone plates for x rays and the extreme UV," J. Opt. Soc. Am. **64**(3), 301–309 (1974).

12. J. Maser and G. Schmahl, “Coupled wave description of the diffraction by zone plates with high aspect ratios,” Opt. Commun. **89**(2-4), 355–362 (1992).
13. G. Schneider, S. Rehbein, and S. Werner, “Volume Effects in Zone Plates,” in *Modern Developments in X-Ray and Neutron Optics*, A. Erko, M. Idir, T. Krist, and A. Michette, eds. (Springer Berlin / Heidelberg, 2008), pp. 137–171.
14. S. Werner, S. Rehbein, P. Guttmann, and G. Schneider, “3-D structured on-chip stacked zone plates for nanoscale X-ray imaging with high efficiency,” Nano Res. **7**, 1–8 (2014).
15. K. Keskinbora, A.-L. Robisch, M. Mayer, C. Grévent, A. V. Szeghalmi, M. Knez, M. Weigand, I. Snigireva, A. Snigirev, T. Salditt, and G. Schütz, “Recent advances in use of atomic layer deposition and focused ion beams for fabrication of Fresnel zone plates for hard x-rays,” Proc. SPIE **8851**, 885119 (2013).
16. Y.-T. Chen, T.-N. Lo, Y. S. Chu, J. Yi, C.-J. Liu, J.-Y. Wang, C.-L. Wang, C.-W. Chiu, T.-E. Hua, Y. Hwu, Q. Shen, G.-C. Yin, K. S. Liang, H.-M. Lin, J. H. Je, and G. Margaritondo, “Full-field hard x-ray microscopy below 30 nm: a challenging nanofabrication achievement,” Nanotechnology **19**(39), 395302 (2008).
17. H. Yan, V. Rose, D. Shu, E. Lima, H. C. Kang, R. Conley, C. Liu, N. Jahedi, A. T. Macrander, G. B. Stephenson, M. Holt, Y. S. Chu, M. Lu, and J. Maser, “Two dimensional hard x-ray nanofocusing with crossed multilayer Laue lenses,” Opt. Express **19**(16), 15069–15076 (2011).
18. H. R. Wu, S. T. Chen, Y. S. Chu, R. Conley, N. Bouet, C. C. Chien, H. H. Chen, C. H. Lin, H. T. Tung, H. H. Chen, G. Margaritondo, J. H. Je, and Y. Hwu, “Nanoresolution radiology of neurons,” J. Phys. D Appl. Phys. **45**(24), 242001 (2012).
19. M. Osterhoff, M. Bartels, F. Döring, C. Eberl, T. Hoinkes, S. Hoffmann, T. Liese, V. Radisch, A. Rauschenbeutel, A.-L. Robisch, A. Ruhlandt, F. Schlenkrich, T. Salditt, and H.-U. Krebs, “Two-dimensional sub-5-nm hard x-ray focusing with MZP,” Proc. SPIE **8848**, 884802 (2013).
20. T. Koyama, H. Takenaka, S. Ichimaru, T. Ohchi, T. Tsuji, H. Takano, and Y. Kagoshima, “Development of Multilayer Laue Lenses; (1) Linear Type,” AIP Conf. Proc. **1365**, 24–27 (2011).
21. T. Koyama, H. Takano, S. Konishi, T. Tsuji, H. Takenaka, S. Ichimaru, T. Ohchi, and Y. Kagoshima, “Circular multilayer zone plate for high-energy x-ray nano-imaging,” Rev. Sci. Instrum. **83**, 013705 (2012).
22. H. Takano, S. Konishi, T. Koyama, Y. Tsusaka, S. Ichimaru, T. Ohchi, H. Takenaka, and Y. Kagoshima, “Point spread function measurement of an X-ray beam focused by a multilayer zone plate with narrow annular aperture,” J. Synchrotron Radiat. **21**(2), 446–448 (2014).
23. X. Huang, H. Yan, E. Nazaretski, R. Conley, N. Bouet, J. Zhou, K. Lauer, L. Li, D. Eom, D. Legnini, R. Harder, I. K. Robinson, and Y. S. Chu, “11 nm hard X-ray focus from a large-aperture multilayer Laue lens,” Sci. Rep. **3**, 3562 (2013).
24. M. Mayer, C. Grévent, A. Szeghalmi, M. Knez, M. Weigand, S. Rehbein, G. Schneider, B. Baretzky, and G. Schütz, “Multilayer Fresnel zone plate for soft X-ray microscopy resolves sub-39nm structures,” Ultramicroscopy **111**(12), 1706–1711 (2011).
25. T. Liese, V. Radisch, I. Knorr, M. Reese, P. Großmann, K. Mann, and H.-U. Krebs, “Development of laser deposited multilayer zone plate structures for soft X-ray radiation,” Appl. Surf. Sci. **257**(12), 5138–5141 (2011).
26. S. Tamura, “Multilayer Fresnel zone plate with high-diffraction efficiency: application of composite layer to x-ray optics,” in *Metal, Ceramic and Polymeric Composites for Various Uses*, J. Cuppoletti, ed. (InTech, 2011), pp. 637–654.
27. F. Döring, A. L. Robisch, C. Eberl, M. Osterhoff, A. Ruhlandt, T. Liese, F. Schlenkrich, S. Hoffmann, M. Bartels, T. Salditt, and H. U. Krebs, “Sub-5 nm hard x-ray point focusing by a combined Kirkpatrick-Baez mirror and multilayer zone plate,” Opt. Express **21**(16), 19311–19323 (2013).
28. R. M. Bionta and K. M. Skulina, “Hard x-ray sputtered-sliced phase zone plates,” MRS Online Proc. Lib. **307**, 343 (1993).
29. D. Rudolph, B. Niemann, and G. Schmahl, “Status of the sputtered sliced zone plates for x-ray microscopy,” Proc. Soc. Photo Opt. Instrum. Eng. **316**, 103–105 (1981).
30. D. Rudolph and G. Schmahl, “High power zone plates for a soft x-ray microscope,” Ann. N. Y. Acad. Sci. **342**(1 Ultrasoft X-R), 94–104 (1980).
31. N. Kamijo, S. Tamura, Y. Suzuki, K. Handa, A. Takeuchi, S. Yamamoto, M. Ando, K. Ohsumi, and H. Kihara, “Fabrication of a hard x-ray sputtered-sliced Fresnel phase zone plate,” Rev. Sci. Instrum. **68**(1), 14–16 (1997).
32. T. Koyama, T. Tsuji, H. Takano, Y. Kagoshima, S. Ichimaru, T. Ohchi, and H. Takenaka, “Development of Multilayer Laue Lenses; (2) Circular Type,” AIP Conf. Proc. **1365**, 100–103 (2011).
33. Z. Cai, Y. Xiao, I. Dragomir-Cernatescu, R. Snyder, Z. Wang, and B. Lai, “Direct Observation of Strain Segregation in ZnO Nanorings Using X-ray Diffraction,” (Argonne National Laboratory (ANL), 2006).
34. R. P. Winarski, M. V. Holt, V. Rose, P. Fuesz, D. Carbaugh, C. Benson, D. Shu, D. Kline, G. B. Stephenson, I. McNulty, and J. Maser, “A hard X-ray nanoprobe beamline for nanoscale microscopy,” J. Synchrotron Radiat. **19**(6), 1056–1060 (2012).
35. G. E. Ice, J. D. Budai, and J. W. L. Pang, “The race to x-ray microbeam and nanobeam science,” Science **334**(6060), 1234–1239 (2011).
36. A. Ruhlandt, T. Liese, V. Radisch, S. P. Kruger, M. Osterhoff, K. Giewekemeyer, H. U. Krebs, and T. Salditt, “A combined Kirkpatrick-Baez mirror and multilayer lens for sub-10 nm x-ray focusing,” AIP Adv. **2**(1), 012175 (2012).
37. J. W. Goodman, *Introduction to Fourier Optics* (Roberts and Company Publishers, 2005).

38. J. R. Fienup, "Reconstruction of an object from the modulus of its Fourier transform," Opt. Lett. **3**(1), 27–29 (1978).
39. R. Follath, J. S. Schmidt, M. Weigand, K. Fauth, R. Garrett, I. Gentle, K. Nugent, and S. Wilkins, "The X-ray microscopy beamline UE46-PGM2 at BESSY," AIP Conf. Proc. **1234**, 323–326 (2010).
40. M. Mayer, K. Keskinbora, C. Grévent, A. Szeghalmi, M. Knez, M. Weigand, A. Snigirev, I. Snigireva, and G. Schütz, "Efficient focusing of 8 keV x-rays with multilayer Fresnel zone plates fabricated by atomic layer deposition and focused ion beam milling," J. Synchrotron Radiat. **20**(3), 433–440 (2013).
41. J. Vila-Comamala, K. Jefimovs, J. Raabe, T. Pilvi, R. H. Fink, M. Senoner, A. Maassdorf, M. Ritala, and C. David, "Advanced thin film technology for ultrahigh resolution X-ray microscopy," Ultramicroscopy **109**(11), 1360–1364 (2009).
42. W. B. Yun, P. J. Viccaro, B. Lai, and J. Chrzas, "Coherent hard x-ray focusing optics and applications," Rev. Sci. Instrum. **63**(1), 582 (1992).
43. S. Werner, S. Rehbein, P. Guttmann, S. Heim, and G. Schneider, "Towards high diffraction efficiency zone plates for X-ray microscopy," Microelectron. Eng. **87**(5-8), 1557–1560 (2010).
44. H. Rarback and J. Kirz, "Optical Performance of Apodized Zone Plates," Proc. SPIE **0316**, 120–127 (1982).
45. M. J. Simpson and A. G. Michette, "Imaging properties of modified Fresnel zone plates," Optica Acta: International Journal of Optics **31**(4), 403–413 (1984).
46. A. A. Michelson, *Studies in Optics* (Dover Publications, Incorporated, 1995).
47. G. R. Morrison, "Phase contrast and darkfield imaging in x-ray microscopy," Proc. SPIE **1741**, 186–193 (1993).
48. K. Keskinbora, C. Grévent, U. Eigenthaler, M. Weigand, and G. Schütz, "Rapid prototyping of Fresnel zone plates via direct Ga+ ion beam lithography for high-resolution x-ray imaging," ACS Nano **7**(11), 9788–9797 (2013).
49. R. Lizárraga, E. Holmström, S. C. Parker, and C. Arrouvel, "Structural characterization of amorphous alumina and its polymorphs from first-principles XPS and NMR calculations," Phys. Rev. B **83**(9), 094201 (2011).
50. S. P. Adiga, P. Zapol, and L. A. Curtiss, "Atomistic simulations of amorphous alumina surfaces," Phys. Rev. B **74**(6), 064204 (2006).
51. T. Campbell, R. K. Kalia, A. Nakano, P. Vashishta, S. Ogata, and S. Rodgers, "Dynamics of oxidation of aluminum nanoclusters using variable charge molecular-dynamics simulations on parallel computers," Phys. Rev. Lett. **82**(24), 4866–4869 (1999).
52. H. L. Wang, C. H. Lin, and M. H. Hon, "The dependence of hardness on the density of amorphous alumina thin films by PECVD," Thin Solid Films **310**(1-2), 260–264 (1997).
53. J. R. Wank, S. M. George, and A. W. Weimer, "Nanocoating individual cohesive boron nitride particles in a fluidized bed by ALD," Powder Technol. **142**(1), 59–69 (2004).
54. L. F. Hakim, J. Blackson, S. M. George, and A. W. Weimer, "Nanocoating individual silica nanoparticles by atomic layer deposition in a fluidized bed reactor," Chem. Vap. Deposition **11**(10), 420–425 (2005).
55. K. Kukli, M. Ritala, and M. Leskelä, "Atomic layer epitaxy growth of tantalum oxide thin films from $Ta(OC_2H_5)_5$ and H_2O," J. Electrochem. Soc. **142**(5), 1670–1675 (1995).
56. C. Chaneliere, J. L. Autran, R. A. B. Devine, and B. Balland, "Tantalum pentoxide (Ta_2O_5) thin films for advanced dielectric applications," Mater. Sci. Eng. Rep. **22**(6), 269–322 (1998).
57. S. Gorelick, J. Vila-Comamala, V. A. Guzenko, R. Barrett, M. Salomé, and C. David, "High-efficiency Fresnel zone plates for hard X-rays by 100 keV e-beam lithography and electroplating," J. Synchrotron Radiat. **18**(3), 442–446 (2011).
58. E. Nazaretski, H. Yan, J. Kim, K. Lauer, K. Gofron, D. Shu, and Y. Chu, "Development of a 10 nm spatial resolution Hard X-ray Microscope for the Nanoprobe beamline at NSLS-II," Bull. Am. Phys. Soc. **58**, J46003 (2013).
59. Z. Cai, B. Lai, W. Yun, P. Ilinski, D. Legnini, J. Maser, and W. Rodrigues, "A hard x-ray scanning microprobe for fluorescence imaging and microdiffraction at the advanced photon source," AIP Conf. Proc. **507**, 472–477 (2000).
60. Y. Xiao, Z. Cai, Z. L. Wang, B. Lai, and Y. S. Chu, "An X-ray nanodiffraction technique for structural characterization of individual nanomaterials," J. Synchrotron Radiat. **12**(2), 124–128 (2005).
61. W. Chao, P. Fischer, T. Tyliszczak, S. Rekawa, E. Anderson, and P. Naulleau, "Real space soft x-ray imaging at 10 nm spatial resolution," Opt. Express **20**(9), 9777–9783 (2012).
62. S. Rehbein, P. Guttmann, S. Werner, and G. Schneider, "Characterization of the resolving power and contrast transfer function of a transmission X-ray microscope with partially coherent illumination," Opt. Express **20**(6), 5830–5839 (2012).

1. Introduction

X-ray microscopy brings new insights to materials researchers from different fields by adding either a 3rd spatial [1,2] or a temporal [3,4] dimension to materials analysis, both at very high resolution. To carry out either scanning or full-field transmission microscopy with X-rays, one has to focus the radiation in some way; yet focusing of especially hard X-rays (HXR), to nano-sized spots, is no easy task. First viable focusing optics developed for HXR were based on a pair of mirrors with grazing incidence illumination [5] and were developed in the late

1940s by Kirkpatrick and Baez [6]. Recent developments on the Kirkpatrick-Baez Mirrors (KBMs) allow very high resolution [7–9], however, there is still room for improvement until high resolution imaging can be done *via* KBMs.

On the other hand, one of the most successful ways of focusing soft X-rays has been to utilize diffractive optics called Fresnel Zone Plates (FZPs). A FZP is a set of concentric rings with radially decreasing widths according to the zone plate law, $r_n = (n\lambda f + n^2\lambda^2/4)^{1/2}$. These rings constitute the zones of the FZP. The width of the outermost zone, Δr, defines its full-pitch resolution at 1st diffraction order, $\delta_{Rayleigh} = 1.22\Delta r$ according to the Rayleigh criterion [10]. Another important property of FZPs is their diffraction efficiency, DE, which is a function of the energy dependent complex refractive index and the FZP thickness [11] while in certain cases Δr can also have an important impact on the DE (especially for small Δr and large aspect ratio, A_r) [12,13]. The relatively easy handling of FZPs also contributed to their success as it is a single optic which simplifies the alignment procedure to a great extent. Despite the success of FZPs in soft X-ray (SXR) microscopy which was facilitated by developments in the conventional fabrication technique of e-beam lithography (EBL), the development of FZPs for HXR remained challenging due to the need for very high aspect ratios which are usually out of limits of EBL (A_r of up to about 25 is achievable with increasingly complex techniques) [14,15]. Recently, there have been improvements in focusing of HXR *via* various diffractive optics such as, multilayer Laue lenses, lithographic and multilayer FZPs achieving high resolutions and efficiencies [1,16–23]. FZPs based on multilayer fabrication techniques (ML-FZPs) where a fiber core is coated with a multilayer and sliced to deliver the ML-FZP, overcome the problem of achieving a high aspect ratio by the nature of the fabrication method [19,24–32]. During the ML-FZP fabrication, one can advantageously vary the ML-FZP thickness freely, enabling the fabrication of ML-FZPs with very high aspect ratios, *i.e.* high DE, required for HXR. This would be extremely beneficial for materials analysis *via* HXR nanoprobe beamlines, for instance, in micro-nano-diffraction studies [33,34] to determine the crystal structure with high locality, in addition to high resolution imaging and chemical analysis *via* spectroscopic techniques, as multi-modal X-ray imaging is getting more and more important [35].

One important advantage of ML-FZPs is that many of them can be cut out from the same multilayer coated fiber with thicknesses tailored for different energies. In the present work we take advantage of such an approach and demonstrate two high resolution ML-FZP optics with 35 nm Δr, each of which is optimized in thickness for either hard or soft X-rays. In the HXR range the full width at half maximum (FWHM) at the focal spot is deduced from an autocorrelation analysis [36–38] of the far field diffraction pattern of the ML-FZP, which was illuminated by a KBM pair. This analysis indicates a spot size smaller than 30 nm (FWHM) in two-dimensions, theoretically, indicating a half-pitch resolution of sub-15 nm. Furthermore, in the SXR range, a ML-FZP, with a thickness optimized for that energy region, was tested as focusing optic in a state of the art scanning transmission X-ray microscope (STXM) for direct imaging experiments. The experimentally determined cut-off resolution was 21 nm in feature size. Along with the results of the autocorrelation analysis of HXR experiments, the direct imaging results at the SXR range, confirm the functionality of the fabricated ML-FZP for high energies demonstrating the highest resolution imaging ever achieved by a multilayer type Fresnel zone plate.

2. Experimental methods

2.1 Fabrication of the ML-FZPs

ML-FZPs with 35 nm Δr and 38 µm diameter were fabricated by depositing alternating layers of Al_2O_3 and Ta_2O_5 with a total thickness of 4 µm on a 30 µm diameter glass fiber (A2 by SCHOTT AG, Germany) *via* atomic layer deposition (ALD) as described previously [24]. The resulting multilayer coated fibers were cut, *via* a focused ion beam (FIB) system (Nova

#208379 - $15.00 USD Received 17 Mar 2014; revised 18 Jun 2014; accepted 19 Jun 2014; published 23 Jul 2014
(C) 2014 OSA

NanoLab, FEI, The Netherlands) to thicknesses optimized for either hard (HXR-FZP, 5.9 µm thick) or soft X-rays (SXR-FZP, 1.6 µm thick). The ML-FZPs were then transferred onto molybdenum TEM grids. The final polishing of the FZPs was carried out *via* the FIB with successively lower currents until a satisfactory surface quality was reached. In case of the SXR-FZP a Pt beamstop of approximately 21 µm diameter and ~1.9 µm thickness was deposited directly on the glass core *via* focused ion beam induced deposition in the FIB. The diameter of the beamstop was held smaller than the fiber core in order to protect the zones from parasitic Pt deposition but larger than the OSA used in the SXR experiments to block direct light. The parameter overview of the fabricated ML-FZPs is given in Table 1.

Table 1. Summary of the multilayer Fresnel zone plates used as focusing optics at hard and soft X-ray ranges

FZP Type	D [µm]	Δr [nm]	t [µm]	A_r	t_{BS} [µm]	E [keV]	f [µm]	T_{DE} [%]
HXR-FZP	38	35	5.9	~169	n/a	7.9	8581	~20
SXR-FZP			1.6	~46	~1.9	1.2	1288	~4

D: FZP diameter, Δr: outermost zone width, t: FZP thickness (zone height) after cutting/polishing, A_r: aspect ratio, t_{BS}: thickness of the Pt beamstop, E: test energy, f: focal distance at E. T_{DE}: approximate theoretical diffraction efficiency of a corresponding full FZP of thickness at the energy, E, based on bulk crystal densities.

2.2 Hard X-ray range experiments

The focusing performance of the 5.9 µm thick HXR-FZP, was tested at the coherence beamline P10 of Petra III (DESY, Germany) using an undulator type insertion device and equipped with a Si(111) monochromator. Incoming X-rays, with the energy of 7.9 keV, were prefocused to illuminate the FZP by a set of two elliptical KBMs. The HXR-FZP was located out of the KBM focus, approximately 4 cm downstream its focal plane in order to ensure complete illumination. The far field diffraction pattern of the HXR-FZP was collected by a 649 x 487 pixels (172 µm pixel size) Pilatus 300K detector with single photon count detection (Detrics Inc., Switzerland) located 5.1 m away from the FZP. In order to protect the camera from the intense direct beam, an external central stop located in the flight-tube and/or a 50 µm thick Molybdenum foil located prior to the KBM acting as an attenuator could be inserted into the beam path.

2.3 Soft X-ray range experiments

Scanning transmission X-ray microscopy (STXM) was carried out using MAXYMUS [39], a state of the art STXM, located at the UE46-PGM2 beamline of the BESSYII synchrotron radiation facility (Helmholtz Zentrum, Germany). The beamline employs an APPLE II type undulator, a plane grating monochromator and a slit system to coherently illuminate the FZP. The 1.6 µm thick SXR-FZP was mounted as the focusing optic in MAXYMUS where the 1st order focal spot was selected by a 17 µm wide order selecting aperture (OSA) and utilized for microscopy. Prior to the imaging experiments, the alignment of the ML-FZP with respect to the optical axis was carried out *via* an in-house developed 2-axes tilting stage. The alignment was carried out by tilting the SXR-FZP in pitch and yaw until a full ring was observed in the diffraction pattern recorded on the CCD. This alignment process is similar to that described earlier [40]. To determine the resolution, a Siemens star (X30-30-2 Xradia, USA) with specified smallest features of 30 nm, as well as two 500 and 200 nm thick FIB lamellae sliced from a $GaAs/Al_{0.7}Ga_{0.3}As$ multilayer sample (L200, BAM, Germany) [41] with certified layer thicknesses, were positioned at the 1st order focal plane and raster scanned over the focus. Right behind the test object, an avalanche photodiode (APD, S2382 Hamamatsu, Japan) was employed to collect the total transmitted light at each sample position corresponding to the pixel values of the image. The DE of the SXR-FZP was determined using a slightly different setup. In this setup a 4.4 µm pinhole FIB milled in a ~6 µm thick gold film positioned at the 1st order focal plane, raster scanned over a large area covering the focus and an unobstructed

reference region. This way, the intensity at the focus and the incoming intensity over the ML-FZPs active area could be determined in a single experiment and the ratio of two gives the DE.

3. Structure of the multilayer Fresnel zone plate

The combination of Al_2O_3 and Ta_2O_5 is a robust one for the fabrication of a ML-FZP *via* the atomic layer deposition (ALD) technique, as already demonstrated [24]. Alumina and Tantalum(V)Oxide were deposited *via* well-established ALD processes and resulted in sharp layer interfaces [24] and a smooth coverage around the fiber circumference. Two ML-FZPs were cut from the deposited multilayer with thicknesses optimized for the HXR (labeled as HXR-FZP) and the SXR range (labeled accordingly as SXR-FZP). See Table 1 for an overview of the parameters of both FZPs.

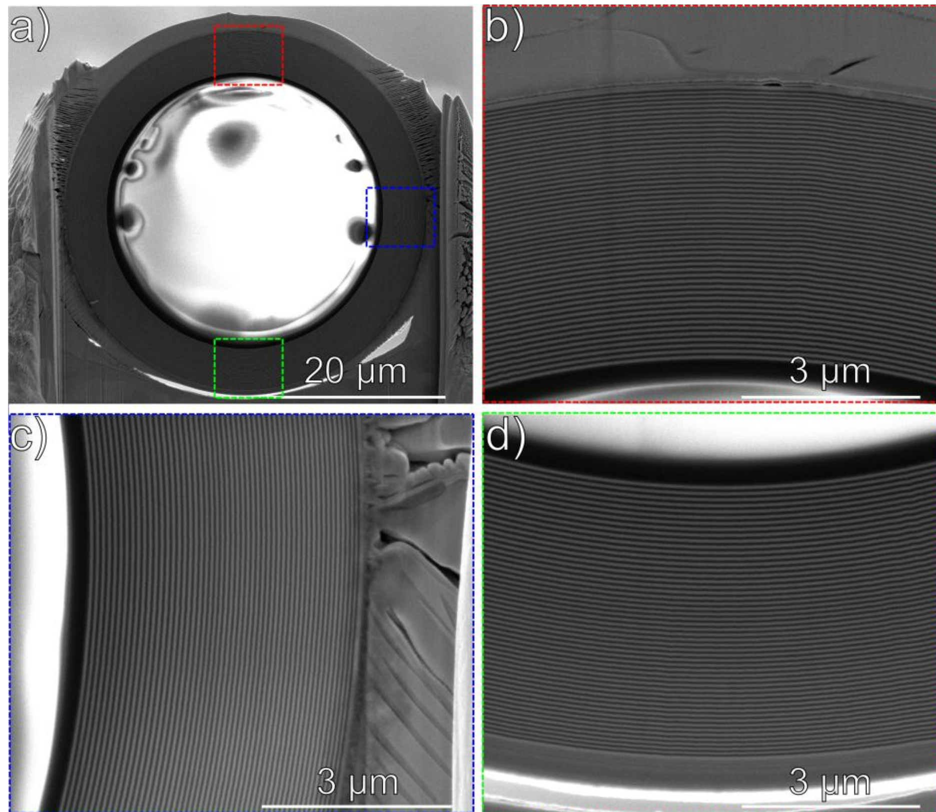

Fig. 1. SEM images of the SXR-FZP prior to beamstop deposition; a) Overview of the SXR-FZP exhibiting the excellent surface quality and homogeneous coverage. Charging in the glass fiber, as a result of the electron bombardment, is responsible for the curvilinear fine structures seen in the core. b-d) higher magnification images from around the FZP. One can see the very well defined layers throughout the multilayer as well as all around the ML-FZP.

Figure 1 shows various regions of the multilayer around the fiber and the resulting ML-FZP structure along with an overview [Fig. 1(a)]. As it can be seen from Figs. 1(b), 1(c) and 1(d), the multilayer interfaces are very well defined. In addition, apart from a few artefacts due to the curtaining effect during FIB preparation, the surface of the ML-FZP is scratch free due to the high precision FIB polishing. An important feature of the ML-FZP shown in Fig. 1(a) is that it has a relatively large diameter (D) of 38 µm, along with a 35 nm Δr, resulting in reasonable focal lengths $(f \approx D\Delta r/\lambda)$ [10] both in the SXR ($f = 1.29$ mm) and the HXR

($f = 8.58$ mm) range (see Table 1). Furthermore, the diameter is small enough to ensure coherent illumination with large flux such that the slit opening which illuminates the ML-FZP can be relatively large. Moreover, the Al_2O_3/Ta_2O_5 combination is quite efficient over a wide energy range, letting the utilization of the ML-FZP at various energies, only by optimizing the thickness of the slice. This is shown in Fig. 2 where the diffraction efficiency (DE) of the Al_2O_3/Ta_2O_5 material system (using bulk crystal densities) is plotted as a function of photon energy and the zone plate thickness according to the thin grating approximation (TGA) [11,42]. The maximum theoretical DE is about 5% in the vicinity of 1.5 keV and increases to more than 20% as the photon energy increases to 8 keV [Fig. 2]. The theoretical DEs for the SXR- and HXR-FZPs tested in this study are 4% at 1.2 keV and 20.8% at 8 keV, respectively (Table 1). These properties provide the structure its versatility and allow focusing high energy radiation at both hard and soft X-rays with high fidelity.

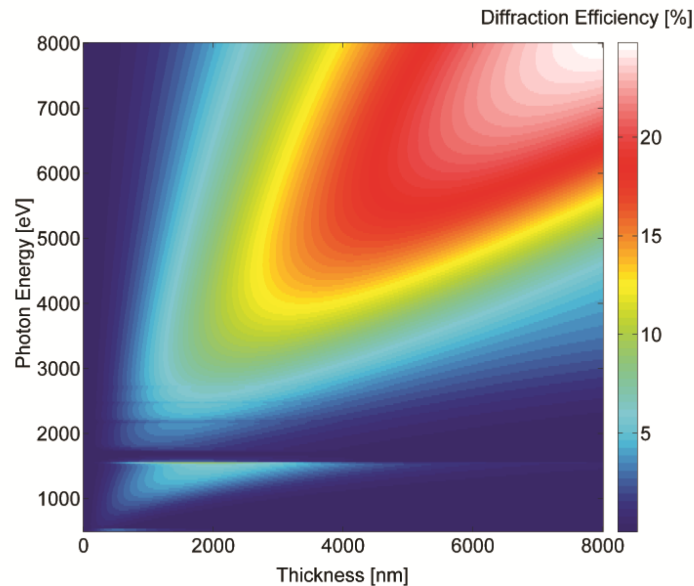

Fig. 2. The diffraction efficiency map of the multilayer Fresnel zone plate made out of Al_2O_3 of 3.95 g/cm^3 density and Ta_2O_5 of 8.2 g/cm^3 density (bulk crystalline densities), calculated according to the TGA. Note that the structure gives reasonable diffraction efficiency even down below 1 keV and increases well above 20% at 8 keV. Two important absorption edges, one at ~1555 eV and one at ~1710 eV, are due to Al K-edge and Ta M-edge, respectively.

4. Focusing hard X-rays

ML-FZPs can be fabricated with very high aspect ratios (A_r) that are required for efficient (up to >15% [40]) focusing of HXR. Despite the proposed improvements in the EBL for increased A_r [14,43], aspect ratios in the order of 10^2 are achievable, so far, only for ML-FZPs [15]. Here, the HXR-FZP has an A_r of approximately 169. Combined with the high efficiency of the structure it provides conditions for robust focusing of HXR. In the experimental configuration shown in Fig. 3, a KBM pair was utilized as a pre-focusing optic to concentrate light onto the ML-FZP [Fig. 3(a) and 3(b)] located on a TEM grid [Fig. 3(c)]. The light is further focused by the ML-FZP into a small focal spot the size of which is determined by the Δr of the HXR-FZP [10]. Behind the focus of the KBM/ML-FZP system, the beam propagates 5.1 m within an evacuated flight tube until it is registered by a 2D single photon counting detector. The measurement configuration is detailed in the experimental section.

#208379 - $15.00 USD Received 17 Mar 2014; revised 18 Jun 2014; accepted 19 Jun 2014; published 23 Jul 2014
(C) 2014 OSA

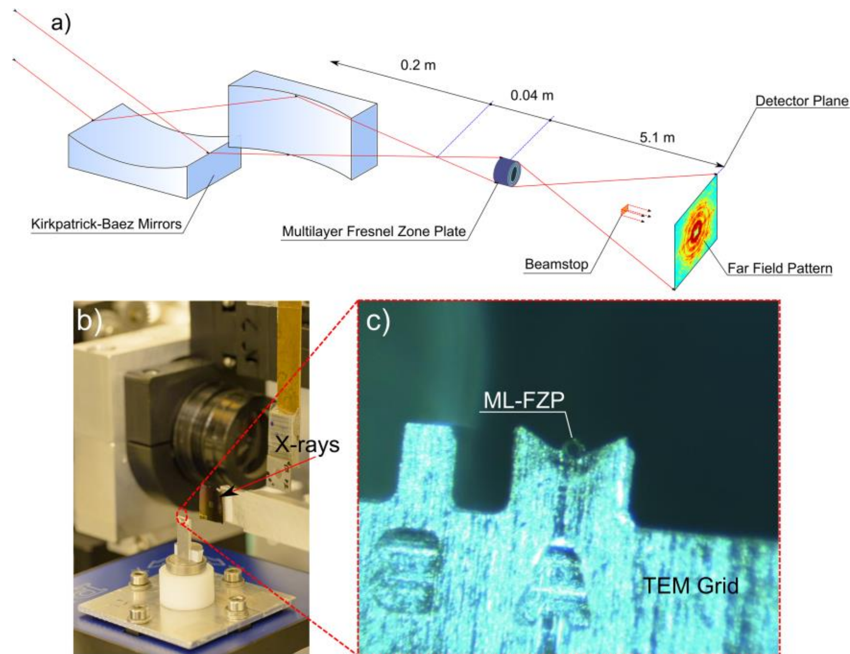

Fig. 3. a) Schematic drawing of the experiment. K-B mirrors were used to collect light and illuminate the ML-FZP. A set of absorbers upstream the K-B mirrors (not shown), as well as a beamstop located downstream in the flight-tube can be used in order to protect the detector from direct light. b) Photographic image of the experimental setup showing the zone plate holder. c) Microscopic image of ML-FZP and the TEM holder on which the zone plate is positioned.

Figure 4(a), recorded while an external beamstop was present in beampath, shows the diffraction rings covering 1st through 3rd order, possibly up to higher orders. The flux at the 1st order focus was calculated by summing up all pixel values of the 1st order diffraction ring and dividing by the exposure time resulting an estimated photon flux of about $4.5\cdot10^{7}$ photons/second. The focal spot size was estimated by an autocorrelation analysis in the following way; the far field diffraction pattern shown in Fig. 4(b), which was recorded while a molybdenum attenuator was inserted in beampath (no beamstop), was used to calculate the autocorrelation function (ACF) at the focal plane which is given in Fig. 4(c). According to the autocorrelation theorem [37] the inverse Fourier transform of a real valued intensity distribution of a two-dimensional field, *e.g.* a far field diffraction pattern, gives the ACF of the source plane, *i.e.* focal plane of ML-FZP, *via* the following relationship;

$$F^{-1}\{G\left|f_X, f_Y\right|^2\} = g(x,y)\otimes g^*(-x,-y) \qquad (1)$$

In Eq. (1), F^{-1} operator is the inverse Fourier transform, f_X and f_Y are spatial-frequency coordinates in the detector plane and x and y are the spatial coordinates in the focal plane. The right hand side of Eq. (1) corresponds to the ACF of the focal plane amplitude while the argument of the inverse Fourier transform, $G\left|f_X, f_Y\right|^2$, on the left hand side corresponds to the far-field diffraction pattern at the detector plane. By means of a simple inverse Fourier transform of the far field diffraction pattern one obtains the ACF at the focal plane. The resulting ACF is given in the Fig. 4(c), and shows a central peak, related to the ACF of the ML-FZP focus, sitting on a broader peak caused by the KBM. The top narrow peak in Fig. 4(c) was isolated and fit with a Gaussian function in x- and y-directions [see Fig. 4(d)]. The full width at half maximum (FWHM) of the ACF of the focal spot was found to be 59×52 nm^2. To connect these values with the spot size in the focal plane, the following aspects have

to be considered: A symmetric far-field intensity pattern $|G|^2$ corresponds to a field distribution with flat phase in the focal plane. Hence, the autocorrelation of the focal field $g(x,y)\otimes g^*(-x,-y)$ should be the same as the convolution of g by itself. For simplicity we assumed the focal field to be of Gaussian shape, and set any remaining flat phase offset to zero. The convolution of a Gaussian function with itself results in a Gaussian function which is broadened by a factor of $\sqrt{2}$. To retrieve the FWHM of the intensity distribution at the focal plane we further have to square the Gaussian function describing the field amplitude, again resulting in another factor of $\sqrt{2}$. Consequently, the FWHM of the focal intensity is by a factor of 2 smaller than the FWHM of the autocorrelation function retrieved from the measured data. This results in a focal spot size of 29.5×26 nm^2. The small difference in the spot size in horizontal and vertical directions could be a result of a slight misalignment with optical axis.

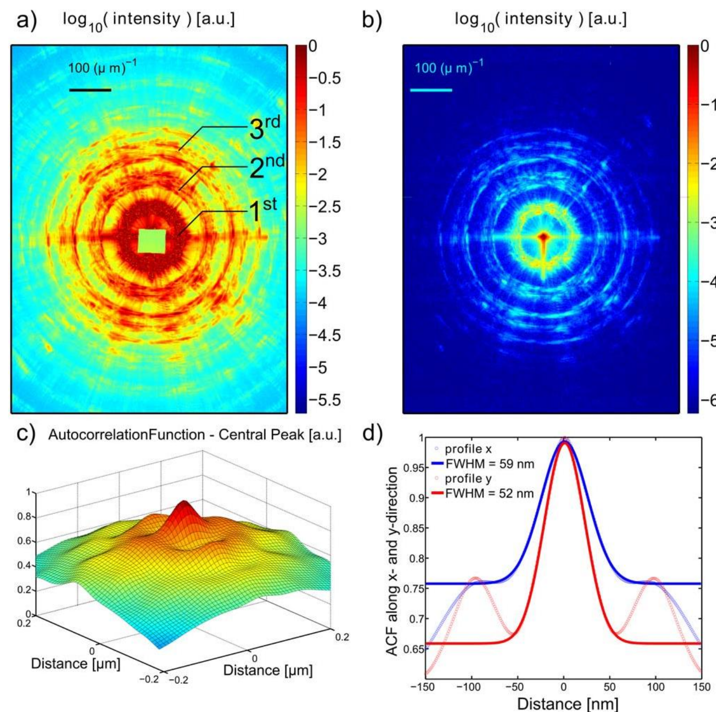

Fig. 4. a) Far field intensity as measured by an area detector with an acquisition time of 100 seconds. One can see the hollow diffraction cones are cut at the detector plane resulting in the 1st, 2nd and 3rd order ring patterns clearly. Acquired while the beamstop was in the beam path and without any attenuator. b) Far field intensity without the beamstop but with a 50 μm thick Mo attenuator prior to the KBM. Scale bars are 100 μm^{-1}. c) 3D representation of the topmost part of the autocorrelation function (ACF) as calculated by an inverse Fourier transform of the far field pattern shown in b. d) The small peak in the center of the autocorrelation function was isolated and fit with a Gaussian along the x- and y- direction. The resulting horizontal and vertical line profiles of the autocorrelation function are plotted here. The FWHM of the Gaussian fits were 59 and 52 nm in the horizontal and vertical direction, respectively.

Complementing the previous analysis we performed a Gaussian surface fit of the autocorrelation. This resulted in a focal size of 33×22 nm^2. The small deviations compared to the one dimensional analysis (29.5×26 nm^2) results from the fact that for the surface fit a plane defines the background level, whereas two independent baselines were chosen for the one dimensional fits.

FWHM values are smaller than the Rayleigh resolution of the present FZP, $\delta_{Rayleigh}$ = 42.7 nm (FWHM≈36 nm) and reflects the specific resolution properties of FZPs with large central stops, sometimes referred to as "apodized" FZPs [44]. This large central stop, composed of the glass fiber core in this case, modifies the Airy pattern [45] of the optic so that the first minimum of Airy pattern shifts from 42.7 nm to approximately 29.9 nm and the FWHM to approximately 27.9 nm. The experimentally determined focal spot size is, therefore, in good agreement with the theoretical expectation. A sub-30 nm full-pitch (FHWM) resolution corresponding to a theoretical sub-15 nm half-pitch resolution can be expected from the optic.

5. Focusing soft X-rays

A scanning transmission X-ray microscope, MAXYMUS [39], was utilized for the experiments in the SXR. Overview of experimental setups for imaging and DE measurements are presented in Fig. 5(a) and 5(b), respectively. Figure 5(a) describes the experimental setup which was utilized for the determination of the spatial resolution. Three samples, a Siemens star with 60 nm smallest periodicity (30 nm feature size) and two lamellae (250 and 500 nm thick) of a multilayer with certified feature sizes (BAM L200 test object), were used as test objects to determine the resolution of the SXR-FZP. Figure 5b illustrates how the DE was determined experimentally. For further details of the setup, samples, beamline and measurement procedures are given in the experimental section above.

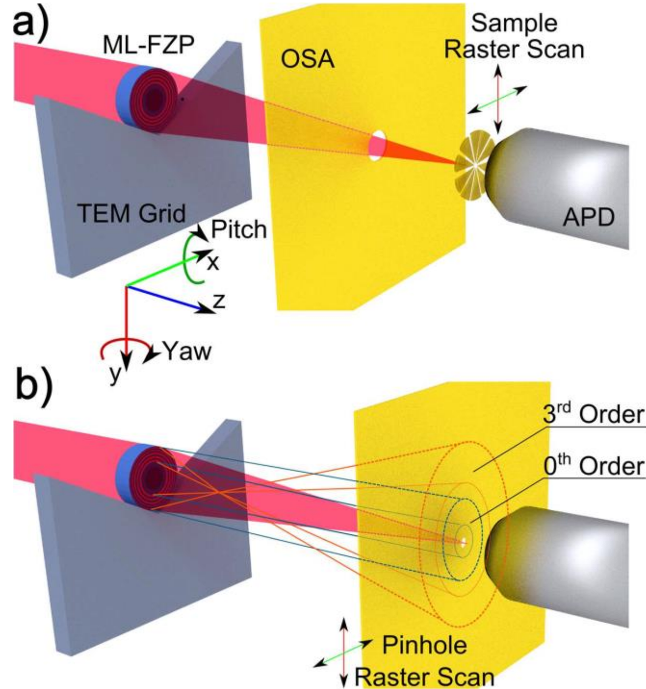

Fig. 5. a) Imaging: the SXR-FZP is shown after alignment. The 1st order focus is isolated by an OSA (17 µm in diameter) positioned between the SXR-FZP and the sample. A test object sample was raster scanned over the focus while the total transmitted light was collected by an avalanche photodiode (APD) to construct the STXM image. b) DE measurement: A smaller pinhole (4.4 µm in diameter) positioned close to the 1st order focal plane is raster scanned across ML-FZP, also covering an unobstructed area serving as a reference to determine the incident light falling on the ML-FZP.

5.1 Imaging using soft X-rays

In the soft X-ray range tests at the MAXYMUS STXM, the alignment of the SXR-FZP with the optical axis was carried out using a 2-axis tilt stage, improving the procedure described

#208379 - $15.00 USD Received 17 Mar 2014; revised 18 Jun 2014; accepted 19 Jun 2014; published 23 Jul 2014
(C) 2014 OSA

earlier [40] and now allowing for the highest reported resolution demonstrated *via* direct imaging, for a ML-FZP. In order to align the SXR-FZP, the far-field diffraction pattern was observed on a CCD camera, while tilting the SXR-FZP about x- and y-axes (pitch and yaw) until the diffraction pattern registered at the CCD was circularly symmetric. Following the alignment, STXM images of a Siemens star could be obtained free of any evident aberrations such as astigmatism. The STXM image in Fig. 6(a), demonstrates that the innermost features with smallest line widths of 30 nm (on average, 60 nm period) were clearly resolved regardless of the direction. Previous reports of similar ML-FZPs at SXR range demonstrated lower resolving powers [24,40] and apparently astigmatic images [15]. These were attributed to one or a combination of the following facts: the absence of a high quality test object [24], a sub-optimal FZP thickness and the lack of a beamstop [40] and most importantly the absence of any means of tilt correction [15,24,40]. The achieved resolution and the lack of astigmatism in Fig. 6(a), indicates that the observed astigmatism reported in those earlier works was the result of the misalignment of the ML-FZPs with respect to the optical axis. The roundness of the fiber core is of prime importance in the ML-FZPs. In the light of earlier work [24] and the fact that the image shown in Fig. 6(a) is free of astigmatism, we conclude the roundness of the fiber used in the fabrication is better than what is required for this particular FZP.

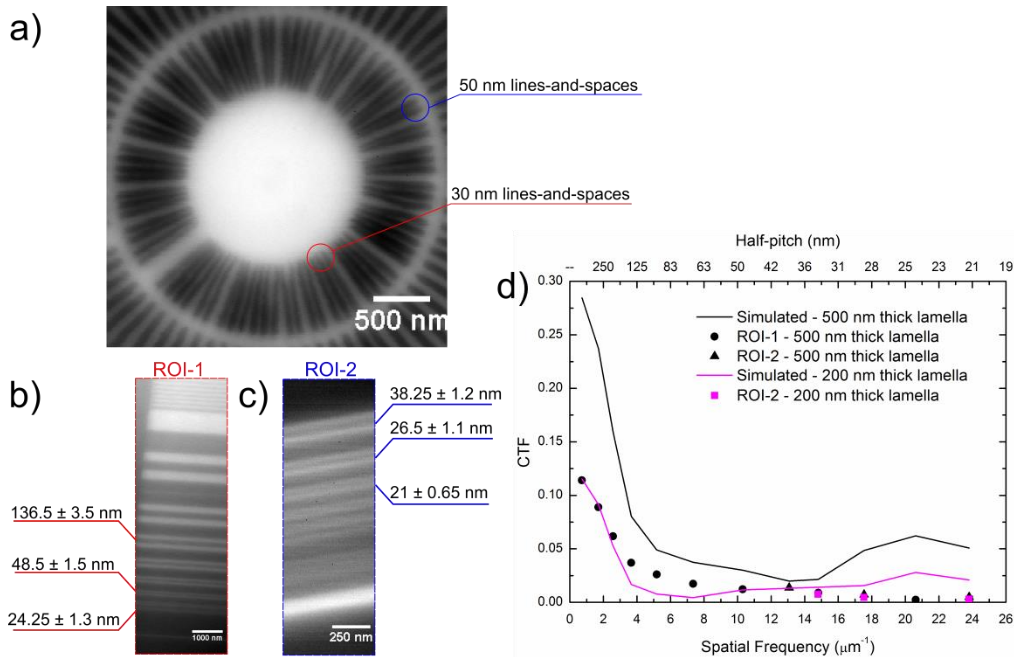

Fig. 6. a) Point by point STXM image of a Siemens star taken at 1 keV with 80 μm vertical and fully open horizontal slits, 10 nm step size and 5 ms pixel dwell time. Given values are average line-and-space distances. b) ROI-1 on the 500 nm thick BAM-L200 sample. Line by line scan, taken at 1.2 keV with 50 μm vertical and full open horizontal slits, 10 nm step size and 1 ms pixel dwell time. c) ROI-2 on the 200 nm thick BAM-L200 sample. Point by point scan, taken at 1.2 keV with 50 x 50 μm slits utilizing, 5 nm step size and 35 ms pixel dwell time. The values given in a) and b) are some of the certified half-pitch sizes and the associated uncertainties. d) The experimental CTFs of the SXR-FZP extracted from the images shown in b) and c) as well as a third image of ROI-2 of the 500 nm thick lamella (not shown) are compared to the simulated CTFs of the SXR-FZP. A mathematical model of test object was convolved with the analytical Airy pattern of the SXR-FZP taking the large central stop into account. Possible imperfect interface profile of the sample was simulated by slightly smoothing the test object.

Note that the imperfections in the innermost part of the Siemens, star due to the lithographic process, result in a varying line-to-space ratio, sometimes significantly less than 30 nm in the smallest features. Accordingly, the feature sizes noted in Fig. 6(a) are average distances. To determine the cut off resolution, a test object with feature sizes in the range of the theoretical resolution limit is required. The BAM-L200 test object fits this requirement very well [41]. In addition, it covers a wide range of structure sizes which can be utilized for the extraction of the contrast transfer function (*CTF*) defined here as the Michelson contrast, $CTF_i = (\mathrm{I}_{\max,i} - \mathrm{I}_{\min,i}) / (\mathrm{I}_{\max,i} + \mathrm{I}_{\min,i})$, where $I_{max,i}$ and $I_{min,i}$ are the highest and lowest pixel values of the local period i [46]. After the alignment of the SXR-FZP with respect to the optical axis, STXM images of the regions of interest (ROI) corresponding to the Fig. 6(b) and 6(c) were recorded. In Fig. 6(c) the 21 ± 0.65 nm lines-and-spaces are clearly resolved. This is by far the best imaging resolution achieved by a multilayer type FZP, to this date. In Fig. 6(d) the experimental *CTF* of the SXR-FZP which was extracted from ROI-1 and ROI-2 is shown along with the simulated *CTFs* estimated from the convolution of the analytical focal spot pattern of the SXR-FZP with the mathematical model of the test object, assuming a coherent illumination of the FZP, a large enough detector and fully absorption contrast imaging resulting in incoherent imaging conditions [47]. *CTF*s decrease with increasing spatial frequency. However, the simulated contrast transfer increases slightly at higher spatial frequencies (most pronounced from 15 to 22 μm^{-1}) due to large central stop. As the *CTF* is very sensitive to the sample under investigation, the thickness of the test object and its transmission profile have direct effects on contrast. The imperfections in the sample such as the presence of an inter-diffusion/inter-mixing between layers (possibly induced during processing or FIB slicing), or even a slight misalignment of the sample with respect to the optical axis may result in a decreased contrast transfer. These influences are included in the simulated *CTF*s as much as possible by taking the transmissivities of the layers into account and by using a limited smoothing to account for the imperfect interfaces. One can see that, for example, the sample with 200 nm thickness results in a less pronounced increase in the *CTF* from 15 to 22 μm^{-1} in comparison to the test sample with 500 nm thickness. The reason that no increase was observed in measured *CTF* in this region may be related to the imperfections within the lens which were excluded in the simulation as only an analytical model of the Airy pattern of a FZP with large central stop was utilized for the calculation. One sees that there is significant contrast transfer down to 21 nm half-pitch. Jumps in the *CTF* of the lens at different ROIs and samples are attributed to the minor changes in sample thickness from ROI to ROI and from sample to sample.

Last but not least, it is worth noting that a second slice of SXR-FZP, cut-out from a different place on the fiber, with ~1.8 μm thickness and without a beamstop (all other parameters same), was also tested using BAM L200 sample. It was also possible to resolve 21 nm features of the BAM L200 sample, albeit at elevated noise level due to lack of a beamstop. In the light of that experiment we conclude that the results are repeatable and the deposition quality of the multilayer structure is homogenous over large distances.

5.2 Diffraction efficiency at soft X-rays

The diffraction efficiency (DE) of the SXR-FZP was measured at several energies ranging from 1000 eV to 1570 eV using a similar procedure described earlier [48]. The experimental DE of the active FZP region (deposited area) was determined to be above 10% between 1550 and 1555 eV while the efficiency of the whole device is 37.7% of this value corresponding to the active area due to the large inactive central obstruction. The change in the intensity in the 1st order focus relative to the incident light at various energies can be seen by analyzing a line scan that was carried out by a 4.4 μm pinhole from 1350 eV to 1675 eV [Figs. 7(a) and 7(b)]. In Fig. 7(b), the recorded intensity shows the diffraction behavior of the SXR-FZP at different energies as well as the amount of light transmitted through the beamstop, the glass fiber core

#208379 - $15.00 USD Received 17 Mar 2014; revised 18 Jun 2014; accepted 19 Jun 2014; published 23 Jul 2014
(C) 2014 OSA

and the 0th order light transmitted through the zones and hence gives a complete picture of the behavior of the optic. Figure 7(b) clearly shows that the intensity at the focal spot (the portion of the image labeled as the 1st order intensity) is especially high near the 1555 eV mark, corresponding to the measured DE behavior plotted as data points in Fig. 7(c). The predicted DE from the calculations based on bulk crystalline densities for the 1.6 µm thick SXR-FZP given in Fig. 2, is overlaid as solid black line in Fig. 7(c). It appears that the measured DE data points lay slightly above this predicted line. The difference is attributed to the amorphous nature of deposited thin films leading to lower densities compared to their bulk counterparts. To account for this variation, DEs were calculated for the same material pair using various theoretical and experimental densities given in the literature for amorphous thin films [49–56]. The mean calculated DE as well as the corresponding standard deviations are shown in Fig. 7(c). The measured values lie within this range and vary from ~3% at 1000 eV to ~10% at 1500 eV, with a maximum of about 12.55% near the Al absorption edge at 1555. These high efficiencies demonstrate, one more time, the high quality zone structure enabled by the ALD process followed by high precision FIB cutting and polishing.

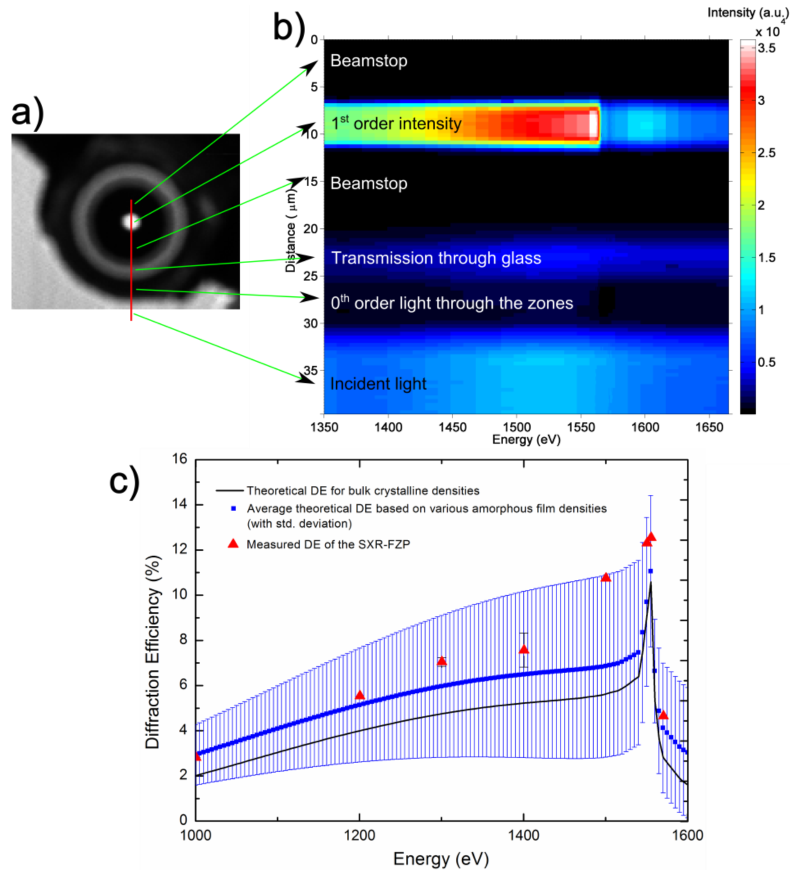

Fig. 7. a) A line by line image scan of the small pinhole (4.4 µm) showing the projection of the light through the different portions of the SXR-FZP. Taken at 1570 eV with 80 µm x open slit, 500 nm step size, 5 ms dwell time. b) A line scan over the 4.4 µm wide pinhole at various energies, utilized for the demonstration of the rapid increase in efficiency near 1550 eV due to the absorption edge of the lens material, namely the Al in Al_2O_3, followed by a rapid decrease. c) Theoretical and experimental diffraction efficiencies as a function of energy for different material densities (bulk and amorphous thin films as detailed in the text). A sharp change in the DE near the aluminum absorption edge, following the calculated value, can be seen in the vicinity of 1555 eV.

#208379 - $15.00 USD Received 17 Mar 2014; revised 18 Jun 2014; accepted 19 Jun 2014; published 23 Jul 2014
(C) 2014 OSA

6. Conclusions

Focusing of high energy radiation *via* utilization of ML-FZPs was demonstrated. The fabrication process is intrinsically capable of delivering FZPs with high efficiency imaging performance at both soft and hard X-rays. The presented ML-FZPs allow for astigmatism free imaging, illustrating both the accuracy of the manufacturing process and the precision of the 2-axes tilt stage specifically developed for the alignment of the optic with respect to the beam and implemented here for the first time. High resolution soft X-ray microscopy with a smallest visible feature size of 21 nm was demonstrated representing the highest direct imaging resolution ever achieved by a ML-FZP to the best of our knowledge. We are convinced that this resolution performance can be extrapolated to the HXR region, as the autocorrelation analysis of the HXR range diffraction experiment supports sub-30 nm full-pitch resolution of the optic. The results show that ML-FZPs are up-and-coming for focusing of hard X-rays to nano-sized focal spots required for direct imaging [1,23,57,58], spectroscopy and for nano-diffraction [33–35,59,60] by using ML-FZPs.

When compared with the conventional FZP manufacturing technique, namely the EBL, ML-FZPs present a number of interesting characteristics. Advantages of EBL-FZPs include currently the highest spatial resolutions among point focusing optics [41,61,62] and easy access to larger diameters in general. They are also conveniently fabricated, *via* well developed schemes, on flat membranes which makes them easier to align. On the other hand, increasing their resolution further seems challenging. EBL-FZPs are limited in aspect ratios and are especially efficient in SXR. In contrast, ML-FZPs can be tailored for a wide energy range by cutting them to the appropriate thicknesses and can be prepared with very high aspect ratios for high efficiency at HXR. Practical difficulties arising from the small diameter of the ML-FZPs with limited focal (*i.e.*, working) distances have to be solved. Addressing this issue leads to work on the optimization of the deposition process for higher deposition rates towards larger diameters. Although the ALD fabricated ML-FZPs are still in their infancy, interestingly, the resolution achieved here in the soft X-ray range is already quite close to that of commercially available EBL-FZPs (usually $\Delta r = 25$ nm). Last but not least, ML-FZPs can potentially reach resolutions beyond current lithographic capabilities as thinner layers of 10 nm and even well below that with high conformality are routinely achievable *via* ALD. This places the technique among the serious potential candidates for ultrahigh resolution (<10 nm) FZP fabrication methods for both soft and hard X-rays. Future perspectives include the optimization of the material selection [40], increased active region and the reduction of the Δr. Demonstration of the best HXR and SXR resolutions, ideally by direct imaging in order to unleash the full potential of these optics remains the ultimate goal.

Acknowledgments

Authors would like to thank to Ulrike Eigenthaler for her help with focused ion beam and to Michael Bechtel for his help with the operation of MAXYMUS and fruitful discussions on the successful deployment of the tilt-stage therein. Finally, feedbacks and inputs from Dr. Stefan Rehbein, Dr. Stefan Werner, Dr. Gerd Schneider from Helmholtz Zentrum Berlin, Dr. Michael Hirscher, Dr. Eberhard Goering and Dr. Herrmann Stoll are gratefully acknowledged.